Experimental Study of a Compressive Line Sensing Imaging System in the Turbulence Environment

BING OUYANG[1*], WEILIN HOU[2], CUILING GONG[3], FRASER R. DALGLEISH[1], FRANK M. CAIMI[1], ANNI K. VUORENKOSKI[1], GERO NOOTZ[5], XIFENG XIAO[4], DAVID G. VOELZ[4]

[1]Harbor Branch Oceanographic Institute, Florida Atlantic University, 5600 US1 North, Fort Pierce, FL 34946;
[2]Naval Research Lab, 1009 Balch Blvd, Stennis Space Center, MS 39529;
[3]Department of Engineering, Texas Christian University, Fort Worth, TX 76129;
[4]Klipsch School of Electrical and Computer Engineering, New Mexico State University, Las Cruces, NM 88003
[5]NRC Research Associate at Naval Research Laboratory, Stennis Space Center, MS 39529

*Corresponding author: bouyang@fau.edu

Received XX Month XXXX; revised XX Month, XXXX; accepted XX Month XXXX; posted XX Month XXXX (Doc. ID XXXXX); published XX Month XXXX

Turbulence poses challenges in many atmospheric and underwater surveillance applications. The compressive line sensing (CLS) active imaging scheme has been demonstrated in simulations and test tank experiments to be effective in scattering media such as turbid coastal water, fog, and mist. The CLS sensing model adopts the distributed compressive sensing theoretical framework that exploits both intra-signal sparsity and the highly correlated nature of adjacent areas in a natural scene. During sensing operation, the laser illuminates the spatial light modulator digital micro-mirror device to generate a series of one-dimensional binary sensing patterns from a codebook to encode the current target line segment. A single element detector photomultiplier tube acquires target reflections as the encoder output. The target can then be recovered using the encoder output and a predicted on-target codebook that reflects the environmental interference of original codebook entries. In this work, we investigated the effectiveness of the CLS imaging system in a turbulence environment. The development of a compact CLS prototype will be discussed, as will a series of experiments using various turbulence intensities at the Naval Research Lab's Simulated Turbulence and Turbidity Environment (STTE). The experimental results showed that that the time-averaged measurements improved both the signal-to-noise radio and the resolution of the reconstructed image in the extreme turbulence environment. The contributing factors for this intriguing and promising result will be discussed.

OCIS codes: (010.0010) Atmospheric and oceanic optics; (010.7060) Turbulence; (110.0110) Imaging system; (140.0140) Lasers and laser optics;

http://dx.doi.org/xxx/xxxxxx

1. INTRODUCTION

1.1. Background

Unmanned aerial vehicles (UAVs) and unmanned underwater vehicles (UUVs) have gained popularity, especially for long-duration surveillance missions, due to their low operation cost and reduced human safety risks. Sensors (e.g., electro-optical [EO] imager) need to be compact and energy efficient to be compatible with the tight resource budgets of such platforms. These constraints are exacerbated when the system operates in degraded visual environments such as fog, turbid coastal water or turbulence. Recent research [1,2] has modeled and demonstrated the effects of turbulence on underwater EO imaging in the natural environment, which confirmed early observations and hypotheses [3]. It seems that turbulence affects imaging transfer in a different manner than turbidity. In turbid water, the absorption reduces all spatial frequencies somewhat evenly. In contrast, turbulence seems to limit imaging capabilities at sharp cut-off frequencies beyond which imaging information is lost. A cumulative, transformational approach different from traditional Fourier domain decomposition might be needed to overcome such challenges. The compressive line sensing (CLS) active imaging system [4,5] was proposed as a possible solution, as well as an energy-efficient alternative to traditional laser line scan (LLS) serial imaging system [6,7]. The non-adaptive serial raster-

scan image formation in an LLS system can be a concern in certain situations. For example, increased platform speeds will require lasers with higher repetition rates to maintain the same image resolution, which inevitably will increase the system cost and require more sophisticated noise mitigation. The CLS system achieves faster image formation, more flexible system configuration and higher energy efficiency. The technique also enables compact and robust system design. The CLS system realizes these advantages by consuming increased computational power during the reconstruction. The system performance has been validated in the strong multi-scattering environment through a series of test-tank experiments [8]. As in many other compressive sensing (CS) imaging applications, the experimental prototype was developed using a digital micro-mirror device (DMD) as the spatial light modulator (SLM).

This paper discusses the experimental study of the CLS system in a controlled optical turbulence environment. Theoretical foundations are discussed in Section 2, and the optical and electronic design of a DMD-based CLS system is described in Section 3. We will discuss the experimental results in Section 4 and the conclusions in Section 5.

2. THEORETICAL FOUNDATIONS

2.1 Turbulence Interference for the Imaging Systems

Optical imaging in the scattering environment is a challenging problem because the channel introduces many types of image-degrading interferences. One of these is turbulence due to pockets of medium of varying temperature, density and index of refraction (e.g., temperature gradients in the deep sea, the air-water boundary). Turbulence layers cause beam spreading and wandering, leading to images distortion and loss of detail. Compared with image degradation caused by turbidity, the varying temporal and spatial nature of turbulence poses a different and perhaps even greater challenge. Optical turbulence can be described by a time and spatial varying modulation transfer function (MTF) [9]. For our subsequent discussions, it is beneficial to re-state some of Fried's results about the instantaneous (un-averaged) MTF and the long exposure time-averaged MTF in the turbulence environment [9].

Considering a spherical wave with radius of curvature R as formed by a plane wave immediately after passing through a thin, diffraction-limited lens of focal length R, then $u(x)$ the phase and amplitude of the image at a point x in the focal plane of the lens, can be approximated by:

$$u(x) \approx A\int dv U(v)\exp\left(-i\frac{2\pi}{\lambda R}v \bullet x\right) \qquad (1)$$

where A is a normalization constant and λ is the wavelength of the light. $U(v)$ is the complex quantity which describes a wave that deviates in amplitude and phase from a spherical wave (in the same manner as the wave collected by the lens that deviates from a plane wave). The image intensity is $I(x) = u(x)u^*(x)$. The MTF can be derived by taking a normalized two-dimensional (2D) Fourier transform of the image intensity. Assuming the incoming wave to have unit amplitude when there is no perturbation, then U can be rewritten as:

$$U(v,t) = W(v)\exp\left[l(v,t) + i\varphi(v,t)\right] \qquad (2)$$

where $W(v)$ is an aperture function that is uniform inside the lens and that vanishes outside of it. $l(v,t)$ and $\varphi(v,t)$ denote the random perturbations of the logarithm of the amplitude and phase, respectively, where t denotes the temporal change. We express U as $U(v,t)$ to indicate the temporal varying nature. In an incoherent imaging system insensitive to the phase variation, the instantaneous MTF is:

$$MTF_I(f) \approx A^2 B\int dv W(v-\lambda Rf)W(v) \exp\left[l(v,t) + l(v-\lambda Rf,t)\right] \qquad (3)$$

where f is the spatial frequency, B is another normalization constant to ensure $\langle \mathrm{MTF}(0)\rangle = 1$ and $\langle\cdot\rangle$ indicates temporal average. l is shown to follow the Gaussian distribution [10] and the variation of l escalates with increased turbulence strength. Assume $\bar{l} = \langle l(v,t)\rangle$ is the mean, then the covariance function is given by:

$$C_l(r) = \left\langle \left[l(v,t) - \bar{l}\right]\left[l(v',t) - \bar{l}\right]\right\rangle \qquad \bar{l} = -C_l(0) \qquad (4)$$

where $r = |v - v'|$. With the log-amplitude-structure function defined as $D(r) = 2[C_l(0) - C_l(r)]$, the long exposure time-averaged MTF can be expressed as:

$$MTF_{LE}(f) = MTF_0(f)\exp\left[-\frac{1}{2}D(\lambda Rf)\right] \qquad MTF_0(f) = A^2 B\int dv W(v-\lambda Rf)W(v) \qquad (5)$$

Adopting the Kolmogorov hypothesis, equation (5) can be simplified [11]:

$$MTF_{LE}(f) = MTF_0(f)\exp\left[-3.44\left(\frac{\lambda Rf}{\rho_0}\right)^{\frac{5}{3}}\right] \qquad (6)$$

where ρ_0 is the Fried parameter or the characteristic seeing parameter that is related to the turbulence strength. Hou proposed a more comprehensive model, the Simple Underwater Imaging Model (SUIM) [1], to describe the underwater scattering in a turbulence environment, which was experimentally validated during the Skaneateles Optical Turbulence Exercise [2].

Comparing equations (3) and (6), the instantaneous MTF provides unstable but possibly broad bandwidth due to the random spatial and temporal variation. A time-averaged MTF provides more stable but narrower bandwidth. These effects are demonstrated in Figure 1 using a video taken with the Extreme Turbulence setting at the STTE facility in Naval Research Lab at Stennis Space Center (NRL-SSC). As the number of frames averaged increases (right column), the image signal-to-noise ratio (SNR) improves, but the edges become more blurry, i.e., the signal resolution decreased due to the reduced bandwidth. With regard to the single frame

image in the left column, there are "lucky" patches where the edge is sharper, but the distortions are more pronounced.

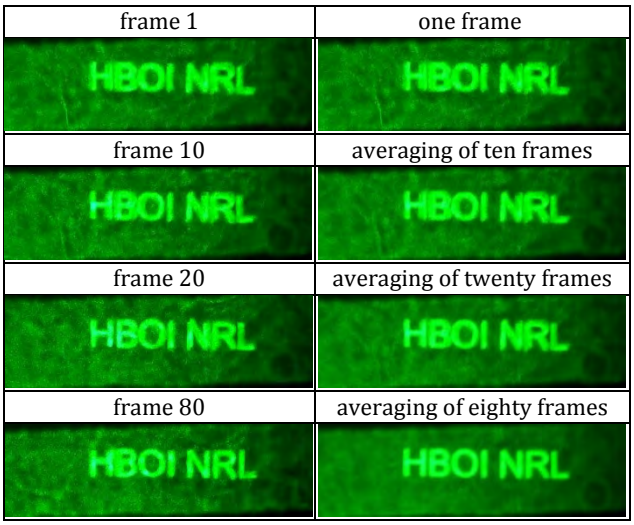

Figure 1. Illustration of the effect of frame averaging using an image sequence taken in the NRL-SSC STTE facility at the Extreme Turbulence setting (10-degree temperature separation). The left side images are single frames extracted from the video; the right side images were produced by averaging the accumulated frames.

2.2 Compressive Sensing and Distributed Compressive Sensing Theories

CS is a framework for the simultaneous sampling and compression of sparse signals using incomplete linear measurements [12,13]. A k-sparse signal $\mathbf{I} \in \mathbf{R^{N\times 1}}$ (i.e., the projection of x on a sparsifying basis $\boldsymbol{\psi} \in \mathbf{R^{N\times N}}$:$\mathbf{I} = \boldsymbol{\psi\alpha}$ contains $\mathbf{K} \ll \mathbf{N}$ non-zero entries) can be recovered with overwhelming probability using more than $\mathbf{M} = \mathbf{O(K\,log N)}$ incoherent linear measurements: $\mathbf{y} = \mathbf{AI} = \mathbf{A\psi\alpha}$ when the measurement matrix $\mathbf{A} \in \mathbf{R^{M\times N}}$ is incoherent with the sparsifying basis $\boldsymbol{\psi}$ and satisfies the restricted isometry property (RIP) [11]. The vector $\boldsymbol{\alpha}$ (and therefore $\mathbf{I}$) can be recovered from the measurements $\mathbf{y}$ by solving an L1-minimization problem.

$$a^* = \arg\min \|a\|_1 \quad subject\ to\ \|y - A\Psi a\|_2 \le \varepsilon \tag{7}$$

The CS theory essentially exploits the intra-signal redundancy within a single source, and there has been significant interest in extending it to cope with the inter-source correlations. One such approach is distributed compressive sensing (DCS) [14]. DCS is closely related to the distributed source coding theorems, which hold that the minimum rate of encoding statistically dependent sources independently is the same as the minimum rate of encoding them jointly, when the sources are decoded jointly and their differences are Gaussian.

DCS attempts to exploit the inter-signal redundancy among distributed and correlated sources through the establishment of the proper joint sparsity models (JSMs) [14]. In JSM-1, the framework adopted in CLS, all sources u_l within the group consist of a sum of a common component Z_c and a component that is unique to each source Z_l: $I_l = Z_c + Z_l$, $l = 0,1 \ldots L$, where L is the number of signals to be solved jointly. On a sparsifying basis Ψ, Z_c and Z_l can be expressed as $Z_c = \Psi\alpha_c$, $\|\alpha_c\|_0 = K_c$, and $Z_l = \Psi\alpha_l$, $\|\alpha_l\|_0 = K_l$ and both are sparse, i.e., $K_c \ll N$ and $K_l \ll N$. The matrix form of the measurement model is illustrated below:

$$\underbrace{\begin{bmatrix} y_1 \\ \vdots \\ y_L \end{bmatrix}}_{\tilde{y}} = \underbrace{\begin{bmatrix} A_1 & & A_1 \\ & \cdots & \vdots \\ & A_L & A_L \end{bmatrix}}_{\tilde{A}} \begin{bmatrix} Z_1 \\ \vdots \\ Z_L \\ Z_c \end{bmatrix} = \underbrace{\begin{bmatrix} A_1 & & A_1 \\ & \cdots & \vdots \\ & A_L & A_L \end{bmatrix}}_{\psi\tilde{\alpha}} \begin{bmatrix} \psi\alpha_1 \\ \vdots \\ \psi\alpha_L \\ \psi\alpha_c \end{bmatrix} \tag{8}$$

where $\tilde{y} = [y(1), \ldots, y(L)]^T \in R^{LM\times 1}$ are the measurements of L sources within the group; $\tilde{\alpha} = [\alpha(1), \ldots, \alpha(L), \alpha_c]^T \in R^{LN\times 1}$ are the coefficients of the sources on the sparsifying basis Ψ, and $\tilde{A}$ is the measurement matrix. Solving such a JSM-1 problem can be cast as L_1-norm minimization with the cost function formulated by revising Equation (7):

$$\tilde{a}^* = \arg\min \|a_c\|_1 + \|a_1\|_1 + \ldots + \|a_L\|_1 \quad subject\ to \left\|\tilde{y} - \tilde{A}\Psi\tilde{a}\right\|_2 \le \varepsilon \tag{9}$$

where $\|\boldsymbol{a}_l\|_1 = \sum_{i=1}^{N} |a_l(i)|$ is the L1-norm of $\boldsymbol{a}_l$.

3. CLS IMAGING SYSTEM ARCHITECTURE

3.1 CLS Signal Model

The CLS illuminator shares some similarity with the streak tube imaging Lidar [15], but instead of a single one-dimensional (1D) fan beam, the illuminator projects a series of 1D fan patterns onto the current target line as shown in Figure 3a. As in many CS imaging systems, this pattern can be generated through modulation of a laser source by an SLM device such as the DMD. Each pattern corresponds to one row in the CS measurement matrix (i.e., codebook). At the receiver, similar to the LLS system, a single element receiver such as the photomultiplier tube (PMT) records the total photon reflection corresponding to the modulation of the spatial pattern with the target as the measurement. Each line on the target is measured independently, and the platform motion enables the line-by-line sensing of the target scene. A group of lines is reconstructed jointly using the DCS JSM-1 model:

$$\tilde{a}^* = \arg\min \|a_c\|_1 + \|a_1\|_1 + \ldots + \|a_L\|_1 \quad subject\ to \left\|\tilde{y} - \Phi\Psi\tilde{a}\right\|_2 \le \varepsilon \tag{10}$$

where L is the number of lines to be solved jointly, Φ is the effective measurement matrix and $\tilde{y}$ are the measurements. Assuming the current line group parameter $L > 1$, then the reconstruction of line r will be included in L solutions. We will buffer these L solutions. The optimum reconstruction for line r can then be derived by averaging or applying a median filter to these L solutions. Interestingly, this unique feature shares similarity with the time delay integration technique [16] that has been used to improve the signal-to-noise ratio of the image sensor readout.

3.2 Mitigating Medium Interference

Several medium interference mitigation techniques are incorporated in the CLS implementation:

- Using patterns that each consists of a group of small beams (i.e. beamlets), instead of area/line flash, to reduce the non-target-bearing photons and using increased beamlet spacing when stronger medium interference presents. Each beamlet pattern in the multi-scaled measurement matrix as shown in Figure 2 contains a small number of beams and satisfies the RIP condition

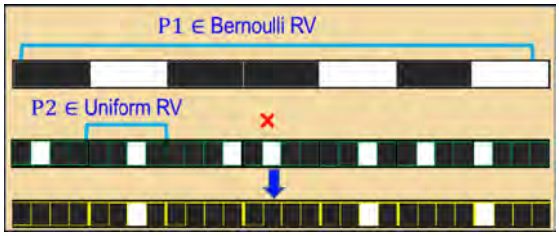

Figure 2. Realization of the multi-scale measurement matrix using the Bernoulli random variable at the top level and the uniform random variable within each block at second level

- Using an "accurate" codebook – predicting the medium impact of the on-target measurement matrices. In this regard, the effective measurement matrix will be: $\Phi = A * PSF_{IT}$. Equation (9) becomes:

$$\begin{aligned} &\tilde{a}^* = \arg\min \ \|a_c\|_1 + \|a_1\|_1 + \ldots + \|a_L\|_1 \\ &subject to \ \|\tilde{y} - \Phi\Psi\tilde{a}\|_2 = \|\tilde{y} - (A * PSF_{IT})\Psi\tilde{a}\|_2 \le \varepsilon, \end{aligned} \quad (11)$$

where $*$ denotes convolution. This is essentially a joint CS reconstruction and (non-blind) deconvolution.

In our current effort of imaging through turbulence, the sensing patterns at the target with distance Z are predicted using the time-averaged point spread function (PSF) [11]:

$$\Phi_m(r,Z) = A_m * PSF(r,Z) = \frac{w_0^2}{w^2(Z)} \sum_{i=1}^{N_m} \exp\left(-\frac{2(r-r_i)^2}{w^2(Z)}\right) \quad (12)$$

where w(Z) is the beam radius at the target and can be expressed as

$$w(Z) = w_0 \left[1 + \left(1 + 2\frac{w_0^2}{\rho_0^2}\right)\left(\frac{2Z}{kw_0^2}\right)^2\right]^{1/2} \quad (13)$$

where ρ_0 is the coherence length of a spherical wave propagating in turbulence:

$$\rho_0 = \left(0.55 C_n^2 k^2 Z\right)^{-\frac{3}{5}} \quad (14)$$

where $k=2\pi/\lambda$ is the wavenumber and C_n^2 is the index of refraction structure constant a parameter describing the turbulence strength. A_m corresponds to the m^{th} entry in the binary codebook {A} and N_m is the number of beamlets in A_m. Φ_m is the corresponding predicted on-target sensing pattern.

Our ultimate goal will be a semi-blind approach where the model prediction will provide the initial state and progressively update both the PSF and the new image content using the new measurements. We plan to add this capability and publish the findings in our future work.

The overall processing framework is illustrated in Figure 3b. The details of the CLS signal model and reconstruction framework have been described previously [5].

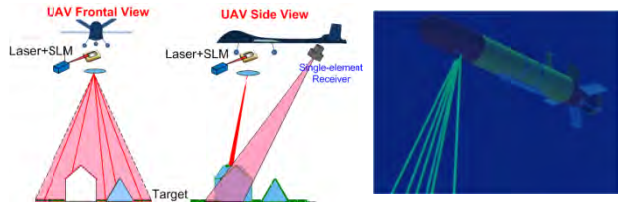

(a) The concept of operations of the CLS imager

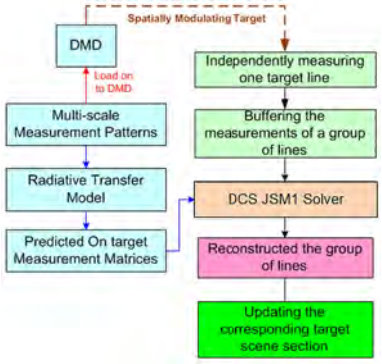

(b) System processing flow

Figure 3. CLS imaging system architecture [5]

3.3 DMD-based CLS Prototype System

The DMD is a micro-electro-mechanical device consisting of millions of electrostatically actuated micromirrors (or pixels) that can be individually controlled to reflect an external light source. Figure 4a shows the light reflection path when the pixels are at ON and OFF states [17].

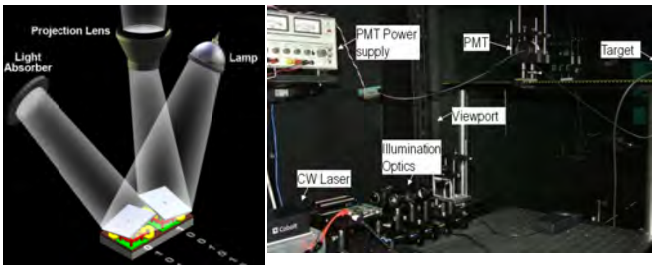

(a) (b)

Figure 4. (a)Illustration of a DMD in binary SLM operation with micromirrors in ON and OFF states [17]; (b) the initial CLS optical bench prototype [18]

The CLS optical bench prototype is shown in Figure 4b. Although adequate for the concept validation effort [18], the system configuration is too cumbersome to be truly considered a "system," and the optical design is not robust and

induces undesirable artifacts. In the current effort, a more compact and robust system was developed. Figure 5 illustrates the new system.

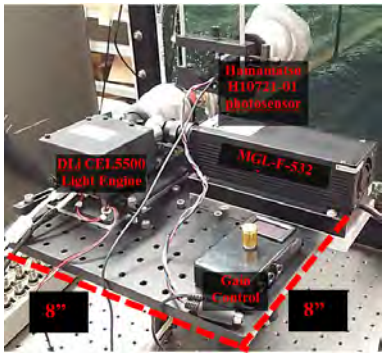

(a) The overall system architecture

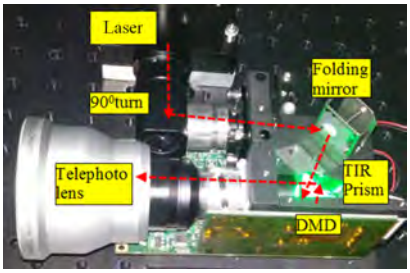

(b) Optical design of the illumination subsystem

Figure 5. The new CLS system

By adopting the Hamamatsu H10721-01 photosensor, the previous bulky power supplies are replaced by a single wall charger and a gain control unit. The illumination source is a CNI MGL-F-532 CW laser with an actual optical output power of 2.88W and four-hour stability of 0.284%. The DLi CEL5500 DMD light engine was adopted as the SLM device. The system now fits on an 8 in. x 8 in. board (Figure 5a). The laser beam is piped into the light engine through a 90-degree angle turn and a custom-made connector to ensure the system is light tight (Figure 5b). A folding mirror directs the beam to the DMD surface. The DMD reflection is re-directed via a total internal reflection prism to the projection path. A 3X telephoto lens is used to generate a field of view (FOV) of 0.5 m at 5 m distance (required for the NRL-SSC test tank). Compared to Figure 4b, the optical path was shortened by more than 75%. These design changes yielded a more compact and, importantly, more robust system. The PMT adopted the same lens to generate an overlapping FOV.

3.4 Motivation to investigate CLS System in the turbulence environment

Imaging through turbulence imposes a different challenge than in a scattering environment [2]. The point spread function in the turbulence environment, in general, is a spatial and temporal variant function. The CLS framework offers some unique features that are worth exploring. Compared with some earlier attempts of CS imaging system in the turbulence environment [19,20], the CLS system does not require sophisticated wave front correction. In the CLS system, the measurement is obtained via spatial encoding of the target and the medium interferences mainly are along the path from the illuminator to the target. By adopting the multi-scaled sensing pattern design, the energy is condensed into a small number of beamlets, which therefore enables improved energy concentration than area flash system [8]. Finally, as mentioned in Section 3.1, one "byproduct" of the CLS framework is a first-in-first-out (FIFO) scheme to store L solutions of each line, (L: the number of lines that are solved jointly). Similar to the time delay integration (TDI) technique, choosing the optimum from the L solutions provides another SNR improvement mechanism.

During this work, we conducted a series of experiments as an initial evaluation of the CLS system in the turbulence environment.

4. EXPERIMENTAL RESULTS

4.1 The Simulated Turbulence and Turbidity Environment at NRL-SSC

The experiments were conducted at the NRL-SCC Simulated Turbulence and Turbidity Environment (STTE) facility, which features a unique 5m Rayleigh-Bénard convective tank (Figure 6a). The stainless steel heat exchanger plates (hot at the bottom, cold at the top) create a controlled, adjustable turbulence environment. The tank can simulate a wide range of turbulence and turbidity observed in nature.

(a) (b)

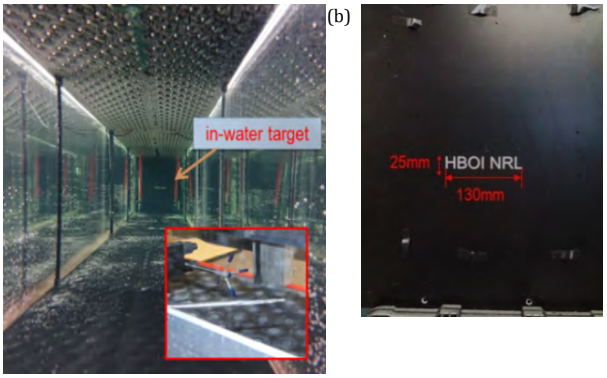

Figure 6. (a) The Rayleigh-Bénard convective tank at the Naval Research Lab, Stennis Space Center (b) The target used in the experiment

4.2 Experimental Setup

During the experiment, the CLS prototype and target (Figure 6b) were placed at opposite ends of the tank. Experimental data were acquired with the test tank operated at three different turbulence strengths:

- Clear Water – no turbulence (for a sanity check)
- Strong Turbulence – 5-degree temperature difference
- Extreme Turbulence – 10-degree temperature difference

Figure 7a depicts the geometry of the experimental configuration. The total beam path length in the turbulence was 10m. The CLS prototype was mounted on a Thorlabs MLJ050 motorized lab jack, capable of 50mm vertical motion.

During the experiment, the DMD light engine was operating at a refresh rate of 1 KHz. For each line, the measurements of 240 patterns were acquired. The same set of patterns was repeated 16 times. The total data acquisition duration for each line was therefore about 4s. The lab jack moved in 1mm increments to acquire data for subsequent lines.

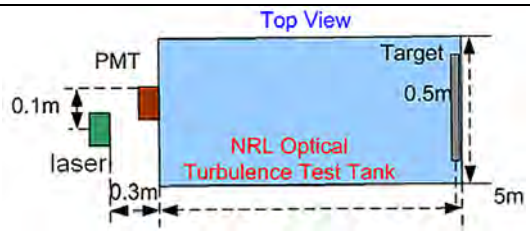

(a) Overall experiment geometry

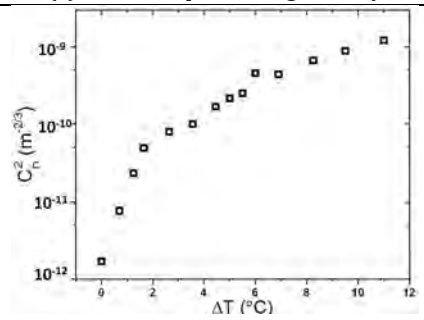

(b) The turbulence strength (C_n^2) as a function of temperature difference of the hot and cold plates

Figure 7. Experimental configuration and test conditions

4.3 Experimental Results

4.3.1. Experimental data processing

During the reconstruction, the time-average PSF in Equation 11 is used to generate the predicted codebook. One of the important parameters in Equation 11 is the coherence length ρ_0, which is related to the turbulence strength parameter C_n^2 through Equation 13. The relationship of C_n^2 and the temperature difference between the hot and cold plates of the NRL-SSC STTE test facility is shown in Figure 7b [21]. The C_n^2 values for Strong and Extreme Turbulences can then be derived as $5e^{-10}$ and $1e^{-9}$ respectively. We assumed C_n^2=$1e^{-10}$ in the Clear Water case.

Based on these measurements, the reconstruction input data for three different scenarios were generated:

- In the "Frozen" case (Figure 8a), one of the 16 cycles (duration = 0.25s) was used as the reconstruction input for each line. This treatment essentially approximates the "frozen turbulence" scenario.
- In the "Binning" case (Figure 8b), a subset from each cycle was extracted and assembled to use as the reconstruction input for each line. This stretched the data acquisition for each line through the 4s duration and amplified the turbulence effect.
- In the "Averaging" case (Figure 8c), the 16 cycles were averaged and used as the reconstruction input for each line.

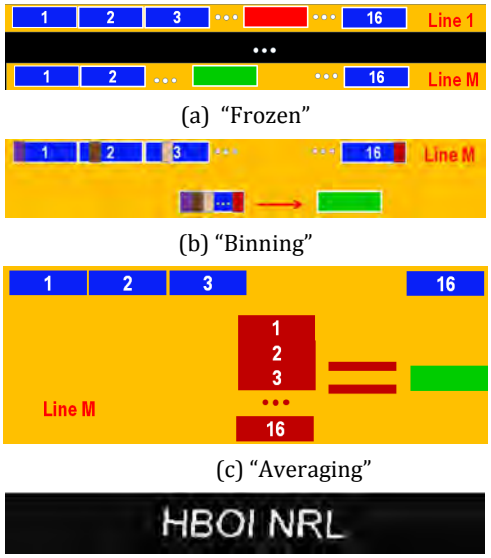

(a) "Frozen"

(b) "Binning"

(c) "Averaging"

(d) Reference image employed in the image quality analysis.

Figure 8. Illustration of the three reconstruction input generation scenarios

The original target was slightly rotated to reflect the imperfect alignment between the CLS illuminator and the target (Figure 8d) and used as the reference for image quality evaluations. An image quality metric that integrates the Structure Similarity Index [22] and the non-referenced image blur metric [23,24]:

$$BSSIM = SSIM * \exp(-BlurMetric) \quad (15)$$

This new metric was to mitigate the SSIM drawback of favoring more blurry and yet "cleaner" (i.e., higher SNR) images [25].

For the image reconstruction, one of the popular basis pursuit solvers, NESTA [26], was adopted. NESTA is a fast and robust first-order method that solves basis-pursuit problems. The total variation (TV) basis was adopted as the sparsifying basis. Enhancements were made so that the TV basis can be compatible with the CLS framework. We will discuss the detail of this enhancement in a subsequent paper. The cross-track (horizontal) image resolution was 384 pixels. Therefore 192 measurements/line would result in a 2:1 compression ratio, whereas 96 measurements/line would result in a 4:1 compression ratio.

We first examine the effectiveness of the predicted codebook by comparing the quality of the reconstruction images using the original binary codebook and the predicted codebook based on Equation 11. Figure 9 presents the BSSIM plots at three different turbulence strengths. The six curves represented the combination of two types of codebook and three types of input treatments described above. Images with a 2:1 compression ratio were used.

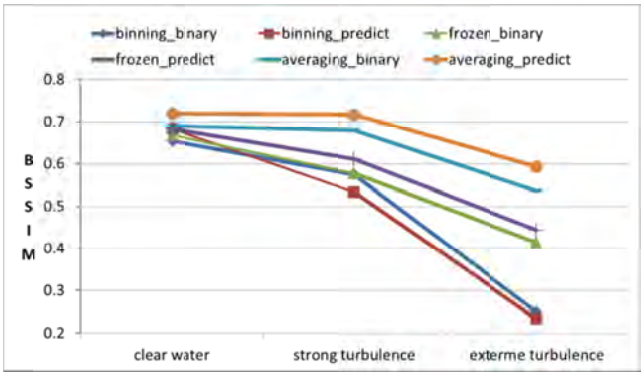

Figure 9. Comparison of binary and predicted codebooks using different input treatments at different turbulence strengths. Images with a 2:1 compression ratio were used.

The Averaging treatment resulted in the most significant improvements followed by the Frozen treatment, with the predicted codebook performing better for both. For the Binning treatment, the predicted codebook performed worse than the binary codebook. Use of the predicted codebook, which essentially incorporates the deconvolution in the reconstruction process, with the Averaging treatment improved the SNR of the measuremnts most, and in turn, enhanced the image quality best.

As an example, Figure 10 presented the reconstructed images at a 2:1 compression ratio for the "Averaging" input treatment at the Extreme Turbulence strength. Visual inspection of these images corroborates the BSSIM metric in Figure 9.

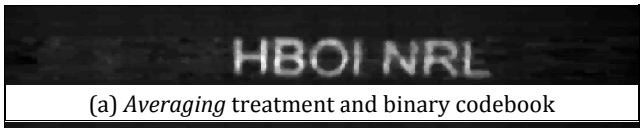

(a) *Averaging* treatment and binary codebook

(b) *Averaging* treatment and predicted codebook

Figure 10. Comparison of reconstructed images at a 2:1 compression ratio for the "Averaging" input treatments at the Extreme Turbulence setting using the binary and predicted codebooks

With the effectiveness of the predicted codebook validated, we provide the reconstruction results using the predicted codebook from here on.

We now examine the performance of the CLS system at different compression ratios, concentrating on the Frozen treatment which corresponds to the real-time measurement acquisition. The BSSIM curves for 2:1 and 4:1 compression ratios at different turbulence strengths are shown in Figure 11a. We present the reconstructed images in Figure 11b, with the background cropped out to provide better visualization. The images in Figure 11b corroborate the BSSIM plots in Figure 11a. The turbulence strength had a significant impact on the image quality. One interesting observation was that the increased compression ratio had a similar impact on image quality as the increased turbulence strength (i.e., Clear Water 4:1 compression ratio vs. Strong Turbulence 2:1 compression ratio).

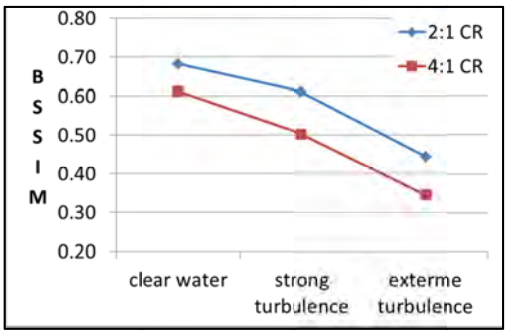

(a) BSSIM plots for 2:1 and 4:1 compression ratios

Strong Turbulence		2:1 compression ratio
		4:1 compression ratio
Extreme Turbulence		2:1 compression ratio
		4:1 compression ratio

(b) Reconstructed images for 2:1 and 4:1 compression ratios at the Strong and Extreme Turbulence strengths

Figure 11. Comparison of the reconstructed images at 2:1 and 4:1 compression ratios for the "Frozen" treatments at different turbulence strengths using the predicted codebook

We now compare the quality of the reconstructed image using three different treatments at different turbulence strengths, which reflects the most exciting and thought-provoking results of this study.

Concerning the image quality hypothesis, our assumptions were that in the Clear Water setting, which can be characterized as a static environment, the Binning and the Frozen cases should perform similarly and Averaging would produce the best result. When imaging through turbulence, Frozen and Averaging would provide similar image quality, with the former generating sharper but noisier images and the latter creating more blurry but cleaner images (i.e., Figure 1 right columns). Both, however, would be better than Binning, where the amplified turbulence effect should significantly degrade the image.

Figures 13a-c show the BSSIM plots for the Clear Water, Strong Turbulence, and Extreme Turbulence settings with the cropped images (2:1 compression ratio) for the different cases superimposed. The results in the Clear Water case followed the hypothesis (Figure 13a) but the results from the two turbulence cases, especially the Extreme Turbulence (Figure 13c), defied it. The Frozen case outperformed the Binning case

as expected, but the fact that the Averaging case produced significantly better BSSIM values (and perceptually sharper and cleaner images) was intriguing. It should be stressed again that this was achieved with the illuminator and receiver co-located. Therefore, the actual laser optical path length was twice the tank length, or 10m.

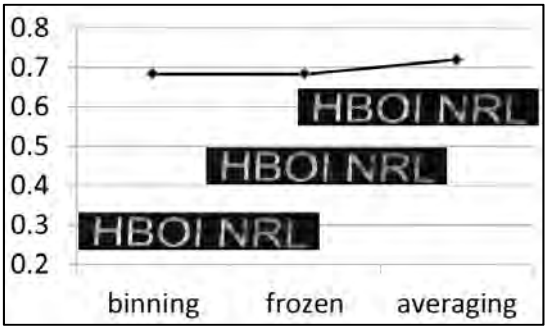

(a) Clear Water

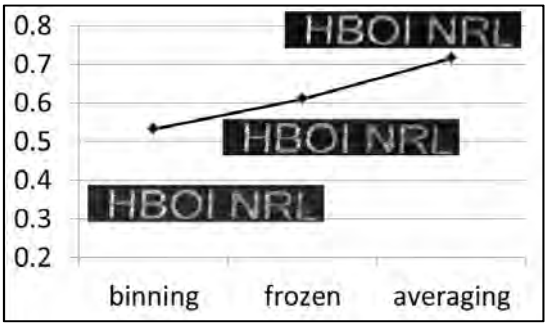

(b) Strong Turbulence

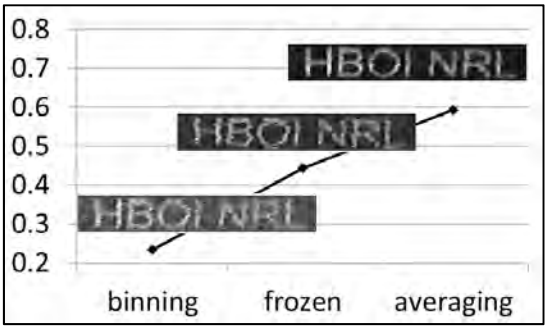

(c) Extreme Turbulence

Figure 13. BSSIM plots for the three settings of Clear Water, Strong Turbulence, and Extreme Turbulence

Two factors may contribute to this performance:

1) Because CLS relies on the spatial encoding of the target to acquire measurements, the medium interferences along the path from the illuminator to the target have more significant impact on the measurements. The propagation from the target to the receiver dispersively attenuates the target reflection. This process reduces the SNR of the measurements but does not significantly alter the "message content." The Averaging process mitigates this reduction, resulting in enhanced image quality.
2) More significantly, in spatial encoding-based CLS measurement acquisition, the measurements encode an entire line instead of measuring individual pixels as with the LLS system or charge coupled device detector. Therefore, another interpretation of the "compression" aspect of the CLS system is that it requires less bandwidth to achieve the required image quality/resolution (Figure 14). The Averaging is essentially a low-pass filtering process. As explained in the Theoretical Foundations section, the increased turbulence strength results in reduced system MTF bandwidth, i.e., channel capacity. Since the CLS system has a lower bandwidth requirement, the reduced channel capacity has less impact on the image quality (blurring) than that of a conventional imaging system.

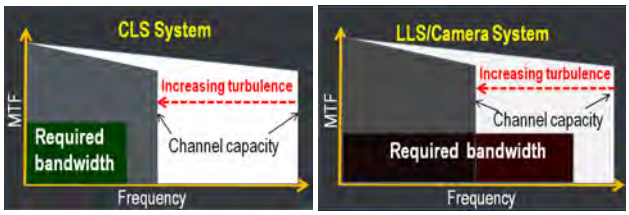

(a) (b)

Figure 14. Illustration of the effect of increased turbulence on the system capacity reduction of the (a) CLS system with "compressed" bandwidth requirement and (b) conventional cameras and LLS system that requires pixel-rate bandwidth. The white trapezoids indicate the channel capacity with no/weaker turbulence; the dark trapezoids indicate the channel capacity with stronger turbulence; the rectangles indicate the bandwidth requirements for different imaging systems.

5. CONCLUSIONS

The overarching goal of this research is to develop a field-deployable CLS imaging system capable of operating in a degraded visual environment. This project is a crucial step in this direction.

This work conveys the first experimental results using the CLS system in a controlled underwater turbulence environment. While we used the underwater turbulence as the surrogate medium, the results are applicable to other environments such as atmospheric turbulence. The performance of the system in extreme-turbulence conditions, especially the significant image quality improvement using the time-averaged measurements, is both intriguing and promising. This finding can be the foundation of a very simple and effective imaging system operating in a turbulence environment. Such a system can be particularly attractive when imaging through turbid and turbulence layers (e.g., the air-sea boundary layer in the coastal zone).

Additional work will be required to fully qualify this finding, such as experimenting with different targets (e.g., target contrast, image content, target material) and system configurations (e.g., different DMD refresh rates, data acquisition durations, receiver placements).

Algorithmically, there are also different areas that require further investigation. The propagation model adopted in this study is the time-averaged model developed for the atmospheric turbulence [11]. While it has been shown to be effective, it will be beneficial to study the SUIM model [1] as an alternative for the underwater environment. Additionally, as mentioned in Section 2, the current reconstruction framework essentially incorporates a non-blind deconvolution component. Extending to a semi-blind deconvolution with the model prediction as the baseline will be an important step.

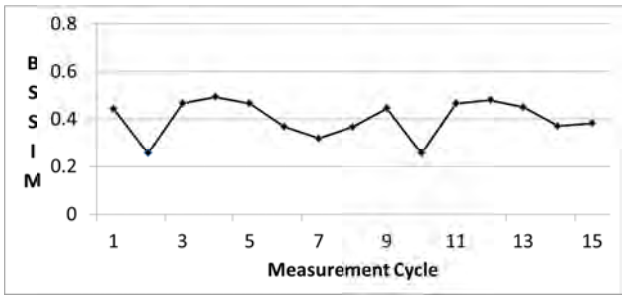

Figure 15. BSSIM plots of the images reconstructed using different individual measurement cycle acquired in the Extreme Turbulence setting, using 2:1 compression ratio

Another interesting aspect that will be investigated in the future is the lucky imaging [27] equivalence in the CLS framework. For this purpose, Figure 15 shows the BSSIM values of the reconstructed images using different measurement cycles. The image quality variation indicates some "lucky" instances exist. One difference is that instead of lucky patches as in the conventional schemes, here what we observed are the "lucky measurements." Therefore, while we currently use all cycles of the measurements in the averaging process, it is highly desirable to average only those lucky measurements to enhance the images further. Investigating a metric to identify these lucky measurements is the key. To this end, the blur metric [24] may be a good starting point.

A related topic that may arise from this work is that this type spatial encoding may be applicable in optical communication through turbulence. In this regard, the message will be first encoded with the CLS measurement codebooks using an SLM device (e.g., DMD). The photons reaching the single element detector (e.g., PMT) will be the encoder output. The code book at the receiver can then be used to decode the message. The robustness of the message can be improved with a time-average process, which was demonstrated to be effective in the experiments mentioned herein.

ACKNOWLEDGEMENT

This work was supported by 2013 AFOSR Young Investigator Program, Naval Research Lab contracts N00173-15-P-0263, ONR grant N000141512195, HBOI Foundation Research Excellence Fund and TCU Invests in Scholarship Fund. The authors thank Dr. Silvia C. Matt, Dr. Damien Josset and Wesley Goode for their help during all phases of experimental tests and Larry Macke for editorial assistance.

REFERENCES

1. W. Hou, "A simple underwater imaging model," Opt. Lett. **34**, 2688-2690 (2009).
2. W. Hou, S. Woods, E. Jarosz, W. Goode, and A. Weidemann, "Optical turbulence on underwater image degradation in natural environments," Appl. Opt. **51**, 2678-2686 (2012).
3. G. D. Gilbert and R. C. Honey, "Optical turbulence in the sea," Proc. SPIE **24**, 49–55 (1972).
4. B. Ouyang, F. R. Dalgleish, F. M. Caimi, T. E. Giddings, J. J. Shirron, A. K. Vuorenkoski, G. Nootz, W. Britton, and B. Ramos, "Compressive Sensing Underwater Laser Serial Imaging System," J. Electron. Imaging **22**, 021010 (2013).
5. B. Ouyang, F. R. Dalgleish, F. M. Caimi, T. E. Giddings, W. Britton, A. K. Vuorenkoski, and G. Nootz, "Compressive Line Sensing Underwater Imaging System," Opt. Eng. **53**, 051409 (2014).
6. J. S. Jaffe, "Computer modeling and the design of optimal underwater imaging systems," IEEE J. Oceanic Eng., **15**, 101-111 (1990) .
7. T. J. Kulp, D. Garvis, R. Kennedy, T. Salmon, K. G. Cooper, "Development and testing of a synchronous scanning underwater imaging system capable of rapid two-dimensional frame imaging," Appl. Opt. **32**, 3520-30 (1993).
8. B. Ouyang, W. Hou, F. R. Dalgleish, F. M. Caimi, A. K. Vuorenkoski, C. Gong, and W. Britton, "Near-infrared compressive line sensing imaging system using individually addressable laser diode array," Proc. SPIE **9484**, 1-12 (2015).
9. D. L. Fried, "Limiting resolution looking down through the atmosphere," J. Opt. Soc. Am. **10**, 1380–1384 (1966).
10. V. I. Tatarski, *Wave Propagation in a Turbulent Medium* (McGraw-Hill, 1961).
11. X. Xiao, B. Ouyang, D. G. Voelz, W. Hou, F. Dalgleish, and A. Vuorenkoski, "Modeling Atmospheric Turbulence Image Reconstruction with Compressive Line Sensing," in *Imaging and Applied Optics 2015*, OSA Technical Digest (Optical Society of America, 2015), paper PM4C.3.
12. E. Candès, J. Romberg, and T. Tao, "Stable Signal Recovery from Incomplete and Inaccurate Measurements," Comm. Pure Appl. Math. **59**, 1207-1223 (2006).
13. D. Donoho, "Compressive Sensing," IEEE Trans. Inform. Theory **52**, 1289-1306 (2006).
14. D. Baron, M. B. Wakin, M. F. Duarte, S. Sarvotham, and R. G. Baraniuk, "Distributed compressed sensing," Rice University, Dept. Electrical and Computer Engineering Technical Report TREE-0612 (2006).
15. Redman, B. C., Griffis, A. J. and Schibley, E. B., "Streak Tube Imaging Lidar (STIL) for 3-D Imaging of Terrestrial Targets," Proc. of 2000 Meeting of the MSS Specialty Group on Active E-O Systems, 11–13 (2000).
16. B. K. Gibson and P. Hickson, "Time Delay Integration CCD Read Out Technique: Image Deformation," Mon. Not. R. Astron. Soc. **258**, 543–551 (1992).
17. D. Dudley, W. Duncan, and J. Slaughter, "Emerging Digital Micromirror Device (DMD) Applications," Proc. SPIE **4985**, 14-25 (2003).

18. B. Ouyang, F. M. Caimi, F. R. Dalgleish, A. K. Vuorenkoski, and W. Hou, “Experimental studies of the compressive line sensing underwater serial imaging system,” Proc. SPIE **9111** (2014).
19. D. Weigel, A. Kiessling, and R. Kowarschik, "Aberration correction in coherence imaging microscopy using an image inverting interferometer," Opt. Express **23**, 20505-20 (2015).
20. J. Polans, R. P. McNabb, J. A. Izatt, and S. Farsiu, “Compressed wavefront sensing,” Opt. Lett. **39**, 1189-92 (2014).
21. G. Nootz, S. Matt, A. Kanaev, and W. Hou are preparing a manuscript to be called “Experimental and numerical study of underwater beam propagation in a Rayleigh–Bénard turbulence tank”.
22. Z. Wang and A. C. Bovik, “A universal image quality index,” IEEE Signal Process. Lett. **9**, 81–84 (2002).
23. D. Q. Bao, “Image blur metric,” http://www.mathworks.com/matlabcentral/fileexchange/24676-image-blur-metric.
24. F. Crete, T. Dolmiere, P. Ladret, and M. Nicolas, "The blur effect: perception and estimation with a new no-reference perceptual blur metric,” Proc. SPIE **6492**, (2007).
25. E. Chebbi, F. Benzarti, and H. Amiri, “An improvement of structural similarity index for image quality assessment,” Journal of Computer Science **10**, 353-360 (2014).
26. J. Bobin, S. Becker, and E. Candès, “NESTA: A Fast and Accurate First-order Method for Sparse Recovery,” California Institute of Technology Technical Report (2009).
27. N. M. Law, C. D. Mackay, and J. E. Baldwin, “Lucky imaging: high angular resolution imaging in the visible from the ground,” Astron. Astrophys. **446**, 739–745 (2006).